

GIANT MOLECULAR CLOUDS IN THE SPIRAL ARM OF IC 342

AKIHIKO HIROTA,¹ NARIO KUNO,^{1,2} NAOKO SATO,³ HIROYUKI NAKANISHI,⁴ TOMOKA TOSAKI,^{1,6} AND KAZUO SORAI⁵

Draft version November 16, 2021

ABSTRACT

We present results of ¹²CO (1–0) and ¹³CO (1–0) observations of the northeastern spiral arm segment of IC 342 with a ~ 50 pc resolution carried out with the Nobeyama Millimeter Array. Zero-spacing components were recovered by combining with the existing data taken with the Nobeyama 45 m telescope. The objective of this study is to investigate the variation of cloud properties across the spiral arm with a resolution comparable to the size of giant molecular clouds (GMCs). The observations cover a $1 \text{ kpc} \times 1.5 \text{ kpc}$ region located $\sim 2 \text{ kpc}$ away from the galactic center, where a giant molecular association is located at trailing side and associated star forming regions at leading side. The spiral arm segment was resolved into a number of clouds whose size, temperature and surface mass density are comparable to typical GMCs in the Galaxy. Twenty-six clouds were identified from the combined data cube and the identified clouds followed the line width-size relation of the Galactic GMCs. The identified GMCs were divided into two categories according to whether they are associated with star formation activity or not. Comparison between both categories indicated that the active GMCs are more massive, have smaller line width, and are closer to virial equilibrium compared to the quiescent GMCs. These variations of the GMC properties suggest that dissipation of excess kinetic energy of GMC is a required condition for the onset of massive star formation.

Subject headings: galaxies: individual (IC342) - galaxies: ISM - galaxies:spiral - ISM:clouds-ISM:molecules

1. INTRODUCTION

The formation of massive star is one of the fundamental processes driving secular evolution of spiral galaxies. The rate of massive star formation in galaxies is considered to be regulated by the formation and the evolution of giant molecular clouds (GMCs), which are progenitors of massive stars. However, the exact processes which drive the formation and the evolution of GMC to initiate massive star formation is still unclear.

GMCs are large cloud complexes with mass of 10^5 to several times of $10^6 M_{\odot}$ and size of 20–100 pc (e.g., Sanders et al. 1985; Solomon et al. 1987; Dame et al. 1986). GMCs comprise roughly 80% of the total molecular mass in the inner Galaxy (Sanders et al. 1985; Solomon et al. 1987). Although the mean volume density of GMCs is as low as $\sim 100 \text{ cm}^{-3}$, there is strong density contrasts inside the GMCs, which make local volume density higher than 10^5 cm^{-3} , which is thought as critical density for the onset of the star formation (e.g., Elmegreen 2002). As formation of dense clump is essential in forming stars, interpretation of the physical process which make a density contrast inside GMC is crucial.

Strong scaling relations between the size and line width of GMCs were found both in the Galactic clouds (e.g., Larson 1981; Dame et al. 1986; Solomon et al. 1987; Heyer & Brunt 2004) and in the extragalactic clouds (e.g., Rosolowsky et al. 2003; Bolatto et al. 2003). The scaling relation holds not only across clouds but also within clouds, suggesting that entire structures of GMCs are strongly governed by supersonic turbulent motion (e.g., Larson 1981; Heyer & Brunt 2004). The supersonic turbulence act in two ways: while it supports the GMCs against global gravitational collapse, it also plays an important role in forming density structures within each GMC (*turbulent fragmentation*, e.g., Vazquez-Semadeni 1994; Padoan & Nordlund 2002). There is an argument that, as a consequence of the fragmentation process, dense cloud cores, which finally collapse into stars, are formed inside GMCs (e.g., Elmegreen 2002; Mac Low & Klessen 2004; Krumholz & McKee 2005), although additional process, such as competitive accretion (Bonnell et al. 2001; Bonnell & Bate 2006), might be also required in massive star formation. An investigation of the dynamical properties of GMCs is important in discussing the formation and evolution processes of GMCs.

Recent molecular cloud studies in the Galaxy indicated that GMCs which lack associated star formation activity are not as unusual as once thought (e.g., Chiar et al. 1994). A comparison of cloud properties between star-forming GMCs and quiescent GMCs is important in addressing what really controls the star formation activity in GMCs. Williams et al. (1994) compared cloud properties between a quiescent cloud (G216-2.6, known as Maddalena’s cloud, Maddalena & Thaddeus 1985) and an active cloud (the Rosette molecular cloud, Blitz & Thaddeus 1980). They showed that the line width is larger in the Maddalena’s cloud than in the

¹ Nobeyama Radio Observatory, Minamimaki, Minamisaku, Nagano 384-1805, Japan

² The Graduate University of Advanced Studies (SOK-ENDAI), 2-21-1 Osawa, Mitaka, Tokyo 181-8588, Japan

³ Student Center for Independent Research in the Science, Wakayama University, Wakayama-shi, Wakayama 640-8510, Japan

⁴ Graduate School of Science and Engineering, Kagoshima University, 1-21-35 Korimoto, Kagoshima, Kagoshima 890-0065, Japan

⁵ Department of Physics / Department of Cosmosciences, Hokkaido University, Kita-ku, Sapporo 060-0810

⁶ Current address: Joetsu University of Education, 1 Yamayashiki-machi, Joetsu, Niigata, 943-8512, Japan

Rosette cloud over every size scale. However, distance degeneracy in observations of Galactic clouds prevents further investigation of the relation between cloud properties and the star formation activity. To overcome this limitation, observations of molecular clouds in external galaxies are crucial.

Early millimeter molecular-line observations in the external grand-design spiral galaxies often found large associations of molecular clouds (e.g., Vogel et al. 1988; Rand 1995; Rand et al. 1999). Mass of those clouds were larger than GMCs by over an order of magnitude (greater than several times of $10^7 M_\odot$) and termed as giant molecular association (GMA) (Vogel et al. 1988). Distributions of those GMAs were found to be coherently offset from associated HII regions and interpreted as representative of the time delay between the formation of those massive clouds and the onset of the subsequent massive star formation (e.g., Rand 1993). By resolving the spatial offsets down to the scale of GMCs, it should be able to investigate the evolution sequence of GMCs which leads to the massive star formation.

We report the results of the observations of the nearby galaxy IC 342 carried out with the Nobeyama Millimeter Array (NMA) in ^{12}CO (1–0) and ^{13}CO (1–0) lines. The observed field covers a $1 \text{ kpc} \times 1.5 \text{ kpc}$ region located in the northeastern spiral arm segments, 2kpc away from the galactic center. At the site, spatial offsets between molecular clouds and star forming regions were previously identified by the Nobeyama 45m telescope observation (Hirota et al. 2010). The prime target of this study is to investigate variation of cloud properties across a spiral arm in IC 342 with a spatial resolution comparable to the size of GMCs ($\sim 50\text{pc}$; Sanders et al. 1985; Blitz 1993).

IC 342 is a nearby spiral galaxy classified as SAB(rs)cd (de Vaucouleurs et al. 1991). The central region of IC 342 harbors starburst activity (e.g., Becklin et al. 1980) and because of the strong millimeter and submillimeter emission from the region, the central region (within $\sim 500\text{pc}$) of the galaxy has been studied in detail. The distributions of molecular clouds is indicative of bar potential (e.g., Ishizuki et al. 1990; Turner & Hurt 1992), and molecular gases are likely to be excited by starburst activity (e.g., Wall & Jaffe 1990; Eckart et al. 1990; Turner et al. 1993; Schulz et al. 2001; Meier et al. 2000; Israel & Baas 2003). Studies of molecular chemistry indicated the chemistry of the clouds in the central region are also subject to shocks (Meier & Turner 2005; Usero et al. 2006) presumably driven by the bar kinematics. Supply of material driven by the bar kinematics is likely to be regulated by negative mechanical feedback from the starburst activity (Schinnerer et al. 2008). Beyond the radius of 500pc , the distribution of the molecular gas disk of IC 342 was studied with the single dish telescope observation mostly in ^{12}CO (1–0) (Sage & Solomon 1991; Crosthwaite et al. 2001; Sato 2006; Kuno et al. 2007). In particular, the ^{12}CO (1–0) map presented in Kuno et al. (2007) reveal prominent galactic structures such as a bar and spiral arms. These structures are also visible in near-infrared images (Jarrett et al. 2003), suggesting the existence of moderately strong density waves in the galaxy. The proximity (3.3 Mpc , Saha et al. 2002) of the galaxy provides an

opportunity to investigate the influence of density waves exerted on molecular clouds.

2. OBSERVATION AND DATA REDUCTION

2.1. ^{12}CO (1–0) and ^{13}CO (1–0) observation

Aperture synthesis observations of the northeastern spiral arm segments of IC 342 in ^{12}CO (1–0) and ^{13}CO (1–0) were carried out with the NMA. The NMA consists of six 10m antennas which provide field-of-view size of $\sim 59''$ and $\sim 62''$ at the rest frequency of ^{12}CO (1–0) and ^{13}CO (1–0), respectively. Three antenna configurations (AB+C+D) were used to sample visibility in the uv range of $\sim 4 \text{ k}\lambda$ to $\sim 130 \text{ k}\lambda$. The observed region covers a GMA located on the northeastern spiral arm segments, where spatial offsets among ^{12}CO (1–0), ^{13}CO (1–0) and star formation tracers exist (Hirota et al. 2010). To cover the region of interest, two pointings separated from each other by $30''$ were set (Figure 1). The ob-

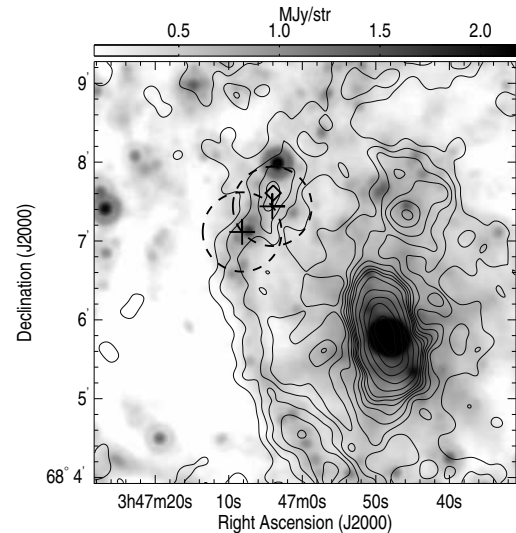


Figure 1. Velocity-integrated image of ^{12}CO (1–0) data taken from Sato (2006) (contour) compared with $24\mu\text{m}$ image taken with the Multiband Imaging Photometer for *Spitzer* (MIPS; Rieke et al. 2004) camera. Contour levels are 10, 15, 20, 25, 30, 35, 40, 50, 70, 100, 140, and 190 K km s^{-1} . Pointing centers of the NMA observations are indicated with crosses. Dashed circles with size of $60''$ indicate approximate size of the NMA field of view ($\sim 59''$ for ^{12}CO (1–0) and $\sim 62''$ for ^{13}CO (1–0)). The peak position of the GMA seen in the ^{12}CO image is indicated with a diamond.

servations were carried out from 2005 November to 2007 April for ^{12}CO (1–0) and from 2006 November to 2007 March for ^{13}CO (1–0). System noise temperatures (in single side band) were 500–1000K for ^{12}CO (1–0) observations and 400–700K for ^{13}CO (1–0) observations. The Ultra-Wide-Band-Correlator (Okumura et al. 2000) configured to cover 256MHz bandwidth with 256 channels was used as the backend. Window function for the spectrometer was set to Hanning smooth function and the resultant frequency resolution was 2MHz. Two pointings were observed alternately every 8 minutes to attain a uniform uv -coverage. B0355+508 was observed once in every ~ 20 minutes as a gain calibrator and 3C273 was observed to determine the pass-band.

Acquired raw visibility data were calibrated using the software package UVPROC-II (Tsutsumi et al. 1997). Though the NMA data were combined with the data observed with the 45m telescope afterward, map image of the CO lines were first made without combining single-dish data to check the basic quality of the data. Imaging and deconvolution were made following the standard procedures implemented in the software package MIRIAD (Sault et al. 1995). Resolution of the resultant ^{12}CO data cube was $3''.1 \times 2''.5$ in spatial directions and 5.2 km s^{-1} in velocity direction. Typical rms noise was $\sim 24 \text{ mJy beam}^{-1}$ within each channel. For ^{13}CO (1–0) data cube, spatial and velocity resolutions were $3''.88 \times 3''.53$ and

$\sim 5.4 \text{ km s}^{-1}$, respectively, and typical rms noise was $\sim 11 \text{ mJy}$ within each channel. The total amount of the flux detected with the NMA is $\sim 8.7 \times 10^1 \text{ Jy km s}^{-1}$ for ^{12}CO (1–0) and $\sim 4.0 \text{ Jy km s}^{-1}$ for ^{13}CO (1–0). While, on the other hand, the total flux emitted from the observed region was estimated from the 45m data and was $\sim 6.1 \times 10^2 \text{ Jy km s}^{-1}$ for ^{12}CO (1–0) and $\sim 8.7 \times 10^1 \text{ Jy km s}^{-1}$ for ^{13}CO (1–0). The large amount of the ‘missing’ flux discrepancies indicates the presence of extended structures whose spatial frequency is lower than $\sim 4.5 \text{ k}\lambda$, which is the minimum spatial frequency available with the NMA.

2.2. NMA and 45m Combined Data: Short Spacing Correction

To recover the missing extended flux, the NMA data were combined with the uv data generated from the 45m data to fill in the central ‘hole’ in the uv -coverage. ^{12}CO (1–0) data were taken from Sato (2006) and ^{13}CO (1–0) data from Hirota et al. (2010). Combining procedures follow the method described in Takakuwa et al. (2003) and Kurono et al. (2009). We will denote outlines of the procedures hereafter. The 45m data were deconvolved with a Gaussian pattern using a Wiener filter and multiplied with the NMA primary beam pattern to simulate the NMA observation. Visibility data were generated from the 45m data by performing Fourier transformation on the deconvolved 45m data. On generating visibility data, (u, v) -sampling points were uniformly distributed within the radius of $4.5 \text{ k}\lambda$, which corresponds to the ‘central hole’ of the NMA (u, v) -coverage. Both the NMA and the 45m visibility data sets were merged to create a single visibility data set and imaged with the inverse Fourier transformation. ‘Clean’ deconvolution was performed with the MOSSDI task implemented in the MIRIAD. Finally, the images were corrected for primary-beam attenuation by dividing with the gain distribution estimated with the standard MIRIAD task (MOSSN). On performing the inverse Fourier transformation, weights attached to the 45m and the NMA visibility determine the shape of the synthesized beam. If larger weights are attached to the 45m data, sensitivity to the low spatial frequency components is increased. However, if the 45m data are overweighted, the shape of the synthesized beam gets close to the 45m beam and thus resolution gets worse.

In practice, the relative weights between the 45m data and the NMA data are determined by the number of the (u, v) -sampling points generated from the 45m data and the integration time attached to each visibility sample

for the 45m data. An adequate choice of the parameters should attain the resolution comparable to the original NMA data and the complete recovery of the missing-flux (Kurono et al. 2009). We generated several sets of visibility data for the 45m data with different integration time attached to each visibility data sample. The number of visibility data points were fixed since only the product of the both parameters is important. Best weight parameter, which satisfies the requirement of the least amount of the missing flux and the least broadening of the beam, was selected from the trial data sets.

Properties of the final combined data cubes are listed in Table 1. Spatial resolutions of the combined data cubes are almost identical to the original data cube. The total flux within the observed fields are also almost identical to the single-dish data within the $\sim 5 \%$ level, which is well below calibration errors.

3. RESULTS

3.1. Molecular gas distribution: ^{12}CO (1–0)

The observed region contains a GMA which was visible with the previous CO observations (Kuno et al. 2007; Hirota et al. 2010). The NMA+45m combined data offer an opportunity to investigate the internal-structure of the GMA with a spatial resolution comparable to the size of GMCs. Figure 2 shows the velocity-integrated intensity image of the combined ^{12}CO (1–0) data. Several discrete sources with sizes of 50–100pc were found. For convenience, three brightest ^{12}CO sources were marked with crosses in the figure (Points 1–3). Indices were allocated in order of the ^{12}CO intensity. Typical brightness temperatures (T_B) at the peaks are 2–4 K above the cosmic background temperature, with a maximum temperature of 5.2 K at Point 1. Although these values are lower than the peak CO temperatures found in Galactic GMCs ($\sim 20\text{K}$), it is comparable with the mean temperature averaged over full extent of cloud. For example, Sakamoto et al. (1994) derived the spectrum of ^{12}CO (1–0) and ^{12}CO (2–1) averaged over almost entire extent of the Orion A and B clouds and presented ^{12}CO (2–1) peak intensities of 1.5K and 2.1K, and CO (2–1) / CO (1–0) ratio of 0.75 and 0.62. These values correspond to ^{12}CO (1–0) temperature of about 2.1K and 3.4K for both the clouds. Comparable brightness temperatures found with the NMA+45m data suggests that clouds seen with our observations may have similar nature with the Galactic clouds.

The characteristics of ^{12}CO distribution on both the southern and the northern sides of the observed fields differ apparently: while it is concentrated in the narrow ridge structure on the southern side, it is more extended on the northern side. On the southern side, the molecular ridge consists of several discrete sources including Points 1 and 2. In a contrasting situation, on the northern side, the cloud distributions are more extended compared to the southern side. The GMA seen as a single peak in the previous 45m image was resolved into several minor peaks around Point 3.

The amount of molecular gas mass is estimated from the CO integrated intensity by applying a ‘‘standard’’ CO– H_2 conversion factor of $X_{\text{CO}} = 2 \times 10^{20} \text{ cm}^{-2} (\text{K km s}^{-1})^{-1}$ (Strong & Mattox 1996; Dame et al. 2001). The

Table 1
Parameters of the Combined CO Data Cubes

Line	Beam Size (arcsec)	Beam Position Angle (deg)	Velocity resolution (km s ⁻¹)	rms Noise (mJy beam ⁻¹)
¹² CO (1–0)	3''.20 × 2''.58	−72°	5.2	23
¹³ CO (1–0)	3''.85 × 3''.53	−69°	5.4	10

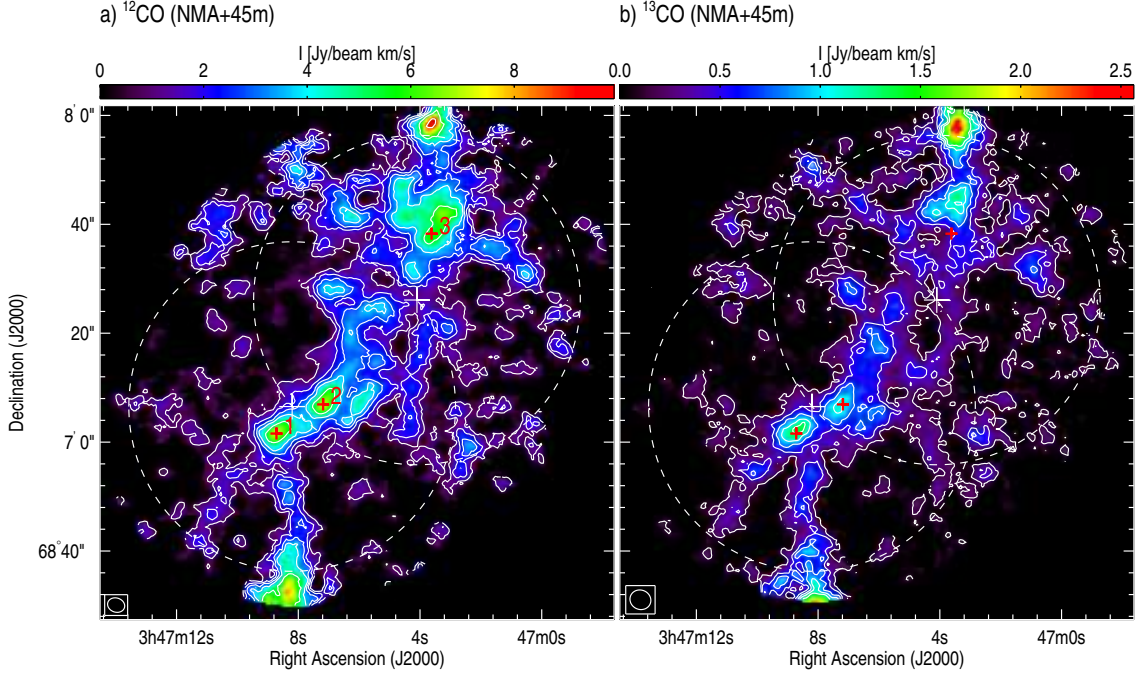


Figure 2. ¹²CO (1–0) and ¹³CO (1–0) integrated intensity images of the northeastern spiral arm segments of IC 342. Locations of the three brightest ¹²CO sources are indicated with crosses (Points 1–3). (a) ¹²CO (1–0) integrated intensity map of the NMA+ 45m combined data. Contour levels are 2, 4, 6, 8, 12, and 20 times 0.45 Jy beam⁻¹ km s⁻¹. Dashed circles indicate the approximate size of the NMA field of view ($\sim 60''$). The attenuation due to the primary beam pattern is corrected. (b) Same as (a), but for the ¹³CO (1–0) data. Contour levels are 1, 3, 5, 7, and 9 times 0.15 Jy beam⁻¹ km s⁻¹.

surface mass density of H₂ is calculated by

$$\left(\frac{\Sigma_{\text{H}_2}}{M_\odot \text{ pc}^{-2}}\right) = 3.21 \times \cos i \times \left(\frac{I_{\text{CO}}}{\text{K km s}^{-1}}\right), \quad (1)$$

where i is the inclination angle of the galaxy ($i = 31^\circ$; Crosthwaite et al. 2000). The surface mass density of molecular gas corrected for He and other heavy elements is derived by

$$\Sigma_{\text{mol}} = 1.36 \times \Sigma_{\text{H}_2}. \quad (2)$$

Highest peak surface molecular gas mass density within the observed region is $\sim 230 M_\odot \text{ pc}^{-2}$ found at Point 1. Typical surface mass densities in other local peaks are $100 - 200 M_\odot \text{ pc}^{-2}$. These are consistent with the value ($\sim 100 M_\odot \text{ pc}^{-2}$) found in the Galactic clouds (e.g., Solomon et al. 1987; Blitz 1993) and several nearby galaxies (e.g., Rosolowsky et al. 2003; Rosolowsky & Blitz 2005). The size, the temperature and the surface mass density of the discrete sources found in the ¹²CO map imply that the NMA+45m observations successfully resolved the molecular spiral arm into individual GMCs.

3.2. Molecular gas distribution: ¹³CO (1–0)

Figure 2(b) shows an integrated intensity map of the combined ¹³CO (1–0) data. To improve the signal-to-noise ratio (S/N) of the integrated image, ¹³CO data were masked before calculating the integrated intensity. The mask data were made according to the following procedures. First, the ¹²CO data cube was smoothed and re-sampled to share the same resolution and pixel coordinates with the ¹³CO data cube. Mask data was made from the smoothed ¹²CO data cube according to the following two-step procedures (Rosolowsky & Blitz 2005): first, pixels above 4σ are adopted as 'kernel' mask and next, all the pixels above 2σ and connected with the 'kernel' are included within the mask. Isolated masks smaller than the beam size were discarded. The applicability of this mask to the ¹³CO data relies on the following issue: as the critical volume density for the excitation of ¹²CO line ($\sim 10^2 \text{ cm}^{-3}$) is much lower than that of ¹³CO line ($\sim 10^3 \text{ cm}^{-3}$), the extent of the ¹³CO emitting volumes should be enclosed within that of ¹²CO emission regions. To check the validity of the mask, intensity histogram of ¹³CO for the residual pixels outside the mask was made. The shape of the residual ¹³CO intensity histogram was symmetric about zero and the central part of the histogram could be fitted with the Gaussian dis-

tribution with a sigma of ~ 11 mJybeam $^{-1}$, which is consistent with the rms noise of the original ^{13}CO data, suggesting that almost all the ^{13}CO emission were enclosed within the mask. Finally, the mask was applied to the original ^{13}CO data cube and integrated intensity was calculated.

While ^{13}CO peaks on the southern side are aligned with ^{12}CO peaks, ^{13}CO peaks on the northern sides are largely deviated from ^{12}CO peaks. In particular, the ^{12}CO sources located around Point 3 (GMA center) lack clear counterpart in ^{13}CO image. As in the case of ^{12}CO , the ^{13}CO distribution on the northern side is spatially extended compared to the southern side.

3.3. Comparison with Multi-wavelength Data

3.3.1. Star formation tracers

The ^{12}CO image was compared with $\text{H}\alpha$, $8\mu\text{m}$, and $24\mu\text{m}$ images to see the spatial relation between the distributions of molecular clouds and star forming regions. Monochromatic $\text{H}\alpha$ image data were provided by Hernandez et al. (2005). Both the $8\mu\text{m}$ image taken with the Infrared Array Camera (IRAC; Fazio et al. 2004) and the $24\mu\text{m}$ image taken with the Multiband Imaging Photometer (Rieke et al. 2004) were retrieved from the *Spitzer* archive. Resolution of the *Spitzer* images is $\sim 1''.2$ for the $8\mu\text{m}$ image and $\sim 6''$ for the $24\mu\text{m}$ image. Figure 3(a)–(c) show the $\text{H}\alpha$ image, the $8\mu\text{m}$ image, and the $24\mu\text{m}$ image respectively. All the images are overlaid with the ^{12}CO (1–0) image.

It is apparent that while the clouds on the southern side are closely associated with their neighboring star forming regions most of the clouds on the northern side seem to lack associated star forming regions. In particular, around Point 3 (center of the GMA), little star formation activities are seen both in the $\text{H}\alpha$ and the mid-infrared images. As we have seen before, the molecular gas distribution around the center of the GMA is much more smooth compared to in the southern side where molecular clouds are concentrated to form the narrow ridge. To see whether such difference of the distribution and star formation activity in both sides of the observed region is related to the properties of clouds, cloud properties will be examined in the latter (Section 4.1).

Previous CO observations made with coarse spatial resolutions (300–1000 pc) often found the well-ordered spatial offsets between the molecular spiral arm and star-forming regions in other spiral galaxies (e.g., Vogel et al. 1988; Rand et al. 1999). Also in IC 342, with the spatial resolution of $\sim 320\text{pc}$, the GMA is seen offset from the star-forming regions (Hirota et al. 2010). While on the other hand, seen with the 50pc resolution here, the separations between the clouds and the associated star-forming regions are small (mostly below the beam size). Recent observations of the grand design spiral galaxy M51 also indicate similar result (Egusa et al. 2011). It is suggested that large GMA found with the previous coarse resolutions is a mixture of the both kinds of clouds, which are clouds associated with and not with star forming region, as in IC 342.

3.3.2. H I

Figure 3 d) shows the comparison between the ^{12}CO image and the H I image. H I data were retrieved from

the Very Large Array archive and reduced with the Astronomical Image Processing System. The resultant H I data cube had a spatial resolution of $23''.2 \times 20''.1$ and typical rms noise of ~ 0.7 mJy beam $^{-1}$ for each channel. The surface mass density of H I is calculated under the assumption of optically thin H I emission. Typical surface density of H I over the observed field is $\sim 2 - 4 M_{\odot} \text{pc}^{-2}$ and is smaller than that of molecular gas by an order of magnitude. Though the spatial resolution of the H I image is $\sim 20''$ and worse than the NMA image, it is apparent that there exists a hole at the center of the GMA. Around the H I hole, distribution of H I roughly coincides with that of H II regions. The coincidence of H I with H II regions indicates that the H I clouds around the GMA might produced by the dissociation of H_2 by the UV radiation.

3.4. Cloud identification and basic cloud properties

To investigate the properties of molecular clouds across the spiral arm, decomposition of individual cloud emission from the combined ^{12}CO (1–0) data was attempted. The CLUMPFIND algorithm (Williams et al. 1994) with some fine-tuning of parameters, which were proposed by Rosolowsky & Blitz (2005), was utilized. Original code of the CLUMPFIND algorithm was targeted at identifying Galactic molecular cloud data observed with single-dish telescopes, in which beam size of the observation is comparable to the pixel size and S/N greatly differs from typical extragalactic observations. Rosolowsky & Blitz (2005) performed cloud decomposition from the interferometric data of M64, which is a molecular rich galaxy with a similar distance to IC 342. They proposed some modifications to be made to the original CLUMPFIND algorithm in applying the algorithm to extragalactic observation data. As the spatial resolution and the S/N of our data resembles that of Rosolowsky & Blitz (2005), we adopted some of the modifications proposed by the author.

The modifications proposed by Rosolowsky & Blitz (2005) consists of two points: one is to alter the manner of locating significant cloud peaks and another is to change distance metric along the velocity axis to account for the oversampling in spatial direction. Among these two modifications, we had adopted only the latter one. In the following, we will briefly mention about the modification we had adopted and not adopted. First, we had adopted the change of distance metric. As the spatial resolution of the combined data is $\sim 3''$ and the cell size of the data is $0.4''$, the data are heavily oversampled in the spatial direction compared to the velocity direction, in which the resolution is $\sim 5.2 \text{ km s}^{-1}$ and the pixel size is $\sim 2.6 \text{ km s}^{-1}$. To account for such oversampling, the distance metric used in the partitioning cloud boundary was modified (see Appendix A of Rosolowsky & Blitz 2005). Second, we tested the modified procedure of finding significant local maxima. While the original CLUMPFIND code searches and partitions data cube into each clump by a fixed intensity interval (usually taken as 2σ), the method proposed by Rosolowsky & Blitz (2005) searches and extends clumps by every 0.5σ but adopt 3σ threshold in discarding 'false' local maxima. We tested the both algorithms and found that the results of the cloud participating are similar to each other, except for clouds around Point 3 (the GMA center). While the original

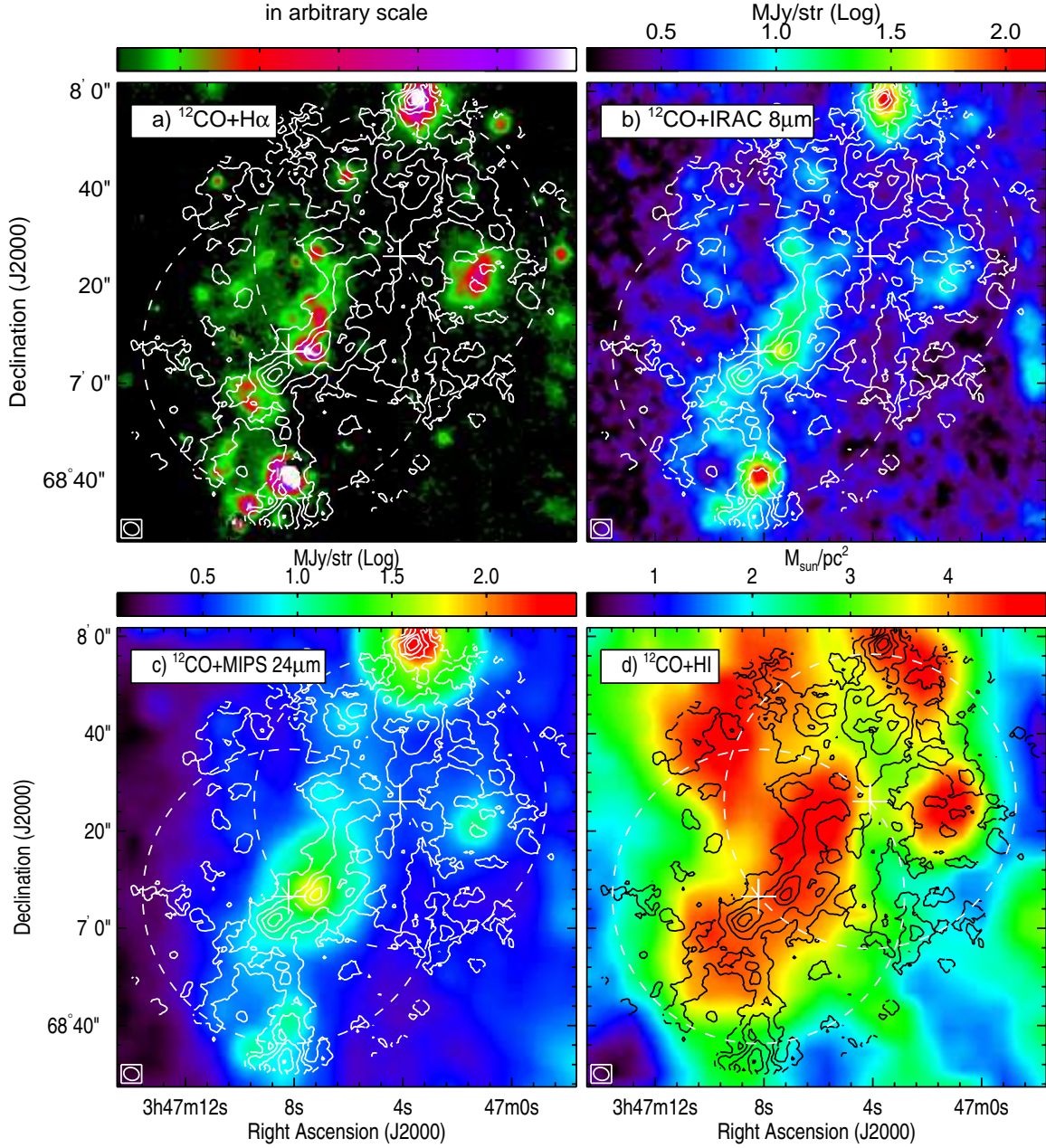


Figure 3. Contour map of the velocity-integrated ^{12}CO (1–0) intensity image overlaid on the pseudocolor scale representations of (a) the $\text{H}\alpha$ image, (b) the $8\mu\text{m}$ image, (c) the $24\mu\text{m}$ image, and (d) the H I image, respectively. Contour levels are 1, 3, 5, 7, and 9 times $1.0 \text{ Jy beam}^{-1} \text{ km s}^{-1}$. Dashed circles indicate the approximate size of the NMA field of view ($\sim 60''$).

CLUMPFIND code produced three clouds around the point, the modified CLUMPFIND algorithm bundled the three clouds into a single large cloud complex. However, close examination of the results indicated that the three clouds bunched by the modified CLUMPFIND algorithm seem to be individual entity because of the different center velocity. Because of this, we did not adopt the modified procedure for finding local maxima in participating the data.

Identification of clouds from the combined NMA+45m data was performed with the following steps. A data cube containing S/N value as a pixel value was generated by dividing the data cube before primary beam correction with rms noise level. The CLUMPFIND al-

gorithm (Williams et al. 1994) with minor modifications mentioned above was applied to the S/N data cube with a 2σ increment level and 2σ lowest cutoff level. After partitioning the data cube into each clump, clumps located completely outside of the primary beam and clumps with peak temperature below 7σ were excluded from the analysis. The 7σ cutoff was set by the fact that over this level, both the algorithms tried here produced similar results, as have noted in the previous. Finally, 26 GMCs were identified from the ^{12}CO data cube. Figure 4 shows locations and approximate extent of the identified clumps projected on spatial directions. Figure 5 shows channel maps of the selected regions from the data cube with peak positions of the identified clumps overlaid, to show

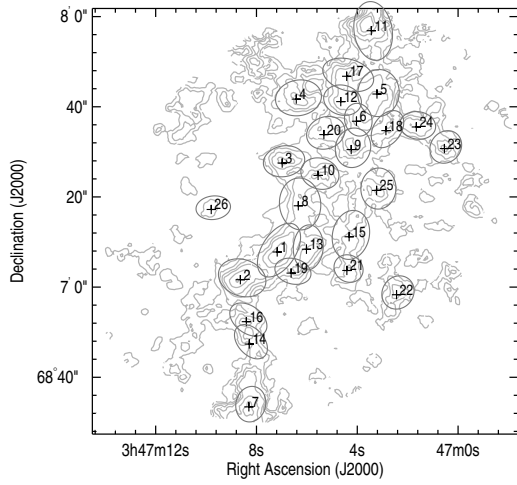


Figure 4. Locations of the identified GMCs overlaid on the velocity integrated ^{12}CO (1–0) image. Contour levels are the same as in Figure 2. Positions of the identified clouds are indicated with crosses. Ellipses indicate the FWHM sizes of the intensity distribution for each cloud. The FWHM sizes and position angle of the ellipses were determined by calculating the eigenvectors of the intensity-weighted covariance matrix for each cloud (see Koda et al. 2006; Rosolowsky & Leroy 2006). Clouds IDs are also indicated on the right of the crosses.

how the identification of the clumps was executed. Properties of the identified clouds, namely, mean position, mean velocity, cloud radius (R), FWHM velocity width (ΔV), and CO luminosity ($L(^{12}\text{CO})$) were measured with the data cube corrected for primary beam attenuation. The mean position and the mean velocity of the clouds were taken as the first moment of the emission. The effective radius of the identified clouds was calculated by

$$R = \frac{3.4}{\sqrt{\pi}} (\sigma_x^2 - \sigma_{\text{beam,maj}}^2)^{1/4} (\sigma_y^2 - \sigma_{\text{beam,min}}^2)^{1/4}, \quad (3)$$

where $3.4/\sqrt{\pi}$ is a factor for converting the rms size into the radius of a spherical cloud (Solomon et al. 1987), σ_x , σ_y is the second moment of the intensity distribution in spatial directions, and $\sigma_{\text{beam,maj}}$ and $\sigma_{\text{beam,min}}$ is the rms size of the observed beam in major and minor axis directions, respectively. As the rms sizes (σ_x , σ_y) are underestimated because of the 2σ clipping level for each cloud boundary, correction should be made. Often used method in this case is a Gaussian correction which assumes a Gaussian profile of the cloud emission and boosts the measured properties with the factor determined by the ratio of the peak temperature to the truncation level (Oka et al. 2001; Bolatto et al. 2003; Rosolowsky & Blitz 2005; Rosolowsky 2007). The correction was made following the analytic expression given by Rosolowsky & Blitz (2005), which boosts the rms size by factor of at most 1.2 for our data. Line width of the clouds was taken as the FWHM size of the cloud profile, also corrected with the Gaussian correction, and corrected for resolution bias by subtracting the velocity resolution ($\sim 2.6 \text{ km s}^{-1}$) in quadrature. CO luminosity was taken as the summation of the emission within

each cloud boundary corrected with the Gaussian correction. Luminosity based cloud mass (M_{CO}) was derived from the CO luminosity by applying the standard conversion factor noted in the previous section (Section 3.1). The virial mass of a spherical cloud with density profile $\rho \propto r^{-n}$ is written as (e.g., MacLaren et al. 1988)

$$\frac{M_{\text{vir}}}{M_{\odot}} = 126 \frac{5-2n}{3-n} \left(\frac{R}{\text{pc}} \right) \left(\frac{\Delta V}{\text{km s}^{-1}} \right)^2. \quad (4)$$

The density profile of $n = 1$ was assumed in calculating the virial mass.

Large scale kinematics of the galactic disk such as the galactic rotation and streaming motions may bias the measured line width and hence the virial mass. To check the possible influence of this, the velocity shear across each cloud was estimated by

$$\Delta V_{\text{shear}}^2 = \frac{\sum I(x_i, y_i) [v_{\text{rot}}(x_i, y_i) - v_{\text{rot}}(x_0, y_0)]^2}{\sum I(x_i, y_i)}, \quad (5)$$

where x_i , y_i is the position of each pixel in the cloud, $v_{\text{rot}}(x_i, y_i)$ is the circular rotational velocity at point (x_i, y_i) , and $v_{\text{rot}}(x_0, y_0)$ is the circular rotational velocity at the mean position of the cloud (x_0, y_0) . An estimated amount of ΔV_{shear} was smaller than the measured line widths by nearly an order of magnitude and turns out to be negligible for our measurement.

Table 2 denotes the basic properties of the identified molecular clouds. The summation of the mass of the identified clouds is $\sim 4.4 \times 10^7 M_{\odot}$, which comprises $\sim 60\%$ of the total molecular mass within the observed region. The relations between the basic properties of the identified clouds are indicated in Figure 6(a)-(d). As the Gaussian correction is the largest source of uncertainty for the measurement of cloud properties, uncorrected values are also indicated for comparison.

3.5. Spatial Relation Between Star Formation Activity and Spiral Arm

The comparison between the ^{12}CO image and the star formation tracers indicated that while some of the clouds seem to lack associated star forming activity, the rest of the clouds are closely associated with accompanying star forming regions. To check whether the properties of the clouds change with associated star forming activity, the identified GMCs were divided into two groups according to their star formation activity.

The H α and the mid-infrared images were examined for the classification. Although the $24\mu\text{m}$ band image is preferable in tracing the star formation rate (Calzetti et al. 2005, 2007), coarse resolution of the $24\mu\text{m}$ image ($\sim 6''$) hampers identification of the correspondence between star-forming regions and the identified clouds. Because of this, the star-forming regions were identified from the IRAC $8\mu\text{m}$ image because of its higher resolution ($\sim 2''$) compared to the $24\mu\text{m}$ image. There is two possible bias in tracing star formation with the $8\mu\text{m}$ image: although the $8\mu\text{m}$ band is dominated by polycyclic aromatic hydrocarbon (PAH) emission mainly excited by photon-dominated region around star-forming regions, there is little but certain amount of stellar contribution to the $8\mu\text{m}$ band (e.g., Helou et al. 2004) and the scaling between the star formation rate and PAH

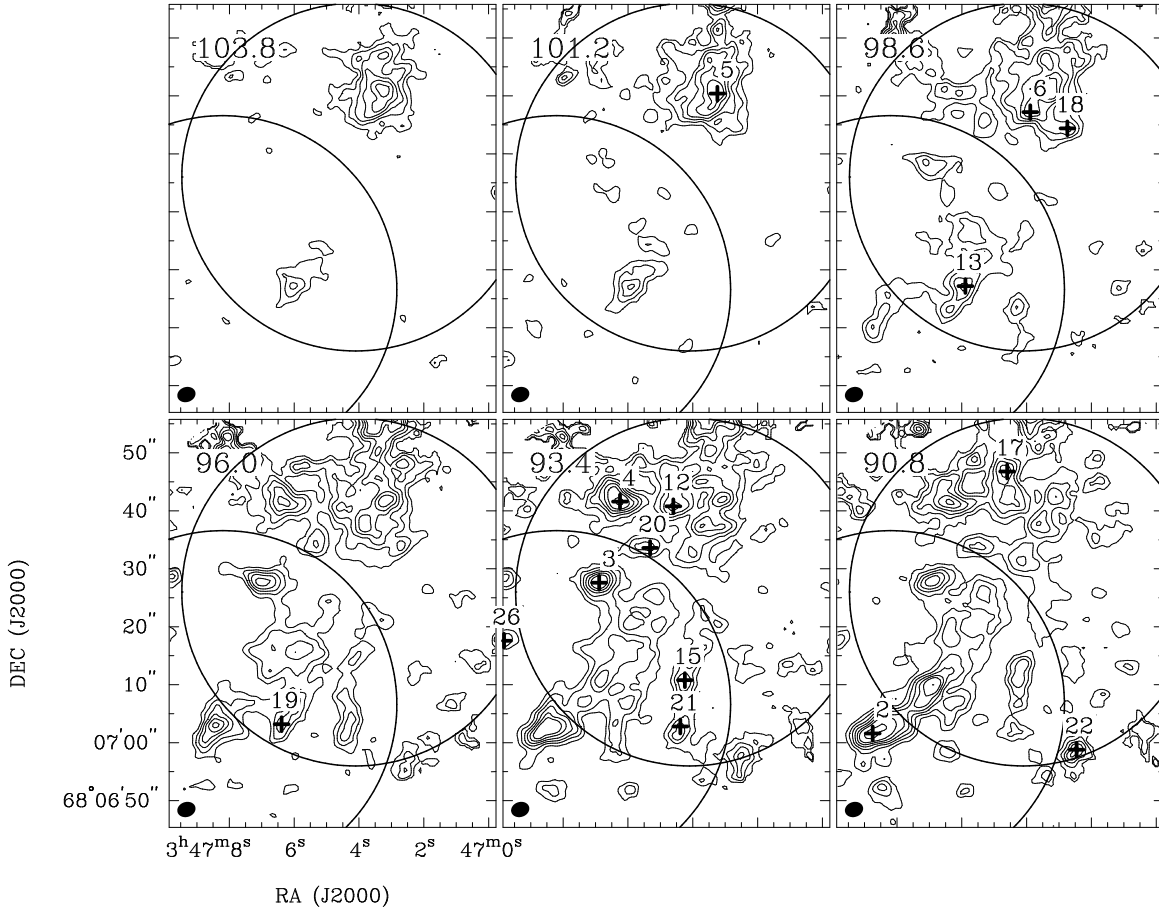


Figure 5. Channel maps of $^{12}\text{CO}(1-0)$ line emission for the selected spatial and velocity range of the data. Peak positions and IDs of the identified clouds are indicated with crosses and associated labels. Contour levels are 4, 6, 8, 10, 12, 14, 18, and 22 times 23 mJy beam^{-1} , respectively. Label on the top left corner of each panel denotes the corresponding center velocity (V_{LSR} in km s^{-1}) for each channel.

emission is slightly deviated from linear possibly because of the presence of diffuse PAH emission excited by ambient radiation field (e.g., Calzetti et al. 2005). However, as we are interested in locating star-forming regions and not in measuring the exact star formation rate, this point is not a severe deficit.

As intensity distribution of star-forming regions seems to have distinct outline, two-dimensional version of the CLUMPFIND algorithm (Williams et al. 1994) was utilized in defying the boundary of each star-forming region. Partitioning of the image was done by every 1.4 MJy str^{-1} ($\sim 2\sigma$) step down to 7 MJy str^{-1} level ($\sim 10\sigma$). The lowest boundary level was determined to keep away from diffuse $8\mu\text{m}$ emission which shall not be related with current massive star formation activity. The distribution of the identified star forming regions was also confirmed by comparing with the $\text{H}\alpha$ image.

The GMCs were divided into two group according to whether they are associated with the identified star forming regions or not. If a GMC overlaps with the identified star forming region and separation between the center of the GMC and that of the associating star forming region is within the beam size, the GMC is categorized as being "associated with star formation". Those "GMCs with H II region" are hereafter referred to as "wHII" GMCs. On the other hand, the rest of the GMCs were categorized as "GMCs without H II region" and termed as

"woHII" GMCs. For most of the "wHII" GMCs, associated star forming regions are seen in both the $8\mu\text{m}$ and the $\text{H}\alpha$ images, except for a GMC located near Point 1. At Point 1, there exists an accompanying bright $8\mu\text{m}$ source but there is no clear counterpart in the $\text{H}\alpha$ image. To qualitatively ensure the classification, $8\mu\text{m}$ flux was measured within the boundary of each cloud. Figure 7 shows a histogram of the measured $8\mu\text{m}$ flux. Although there is a "wHII" GMC which shows exceptionally low $8\mu\text{m}$ flux compared to other "wHII" GMCs (cloud-26), most of the "wHII" GMCs show higher $8\mu\text{m}$ flux compared to the "woHII" GMCs. The low $8\mu\text{m}$ flux for the cloud-26 is due to the fact that the cloud is offset from the associated H II region and the $8\mu\text{m}$ flux is measured only within the cloud boundary. For the rest of the "wHII" clouds, offsets between each cloud and the associated star-forming region are not so large compared to the cloud-26. The $8\mu\text{m}$ flux histogram seems to ensure the classification made here.

Figure 8 shows the spatial distribution of the classified GMCs. As in other grand design spiral galaxies, the spiral arm in IC 342 has an exponential nature; the spiral arm extends almost linearly on the $\log R-\theta$ diagram (Sato 2006; Hirota et al. 2010). Lines of the constant spiral phase ($\theta = 0^\circ, -13^\circ$) are indicated in the figure for comparison. The comparison of the distribution of the GMCs with respect to the spiral phases shows that the

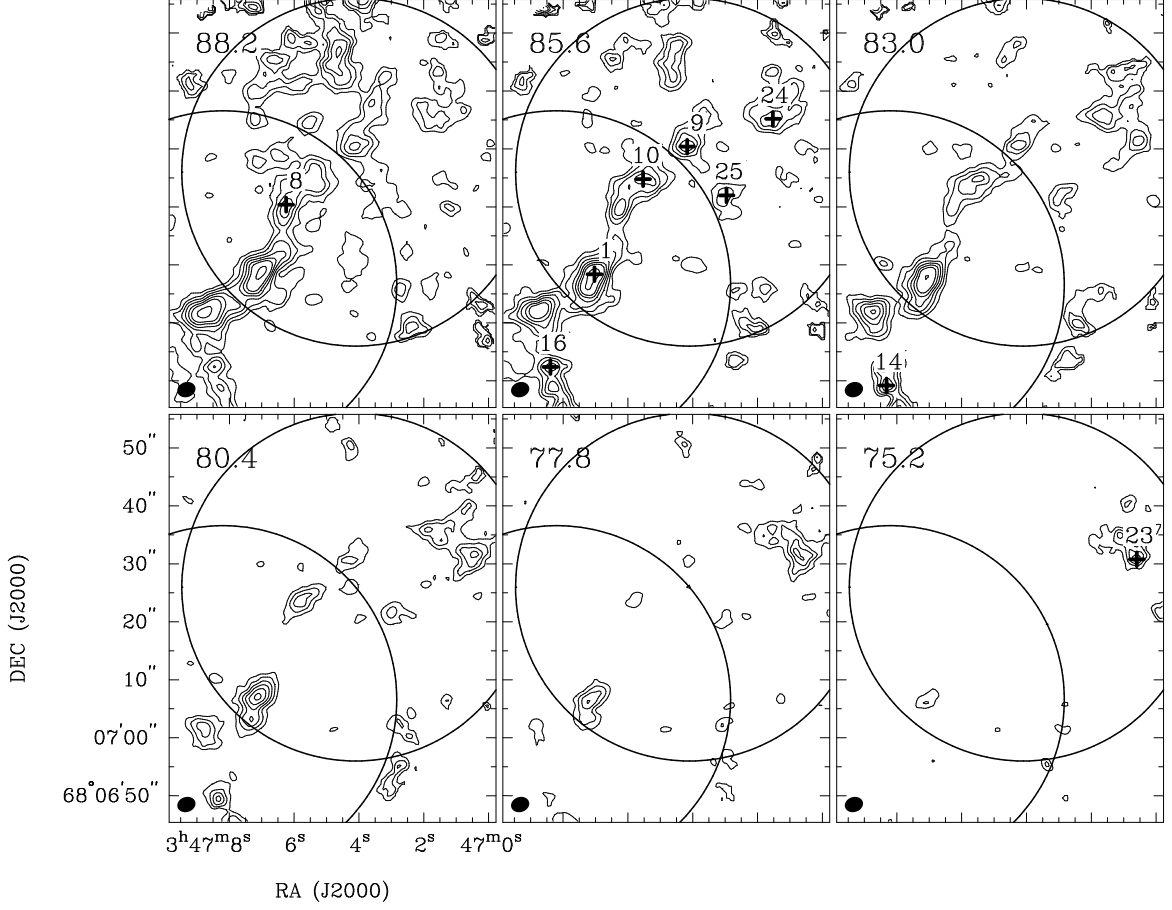


Figure 5. (Continued)

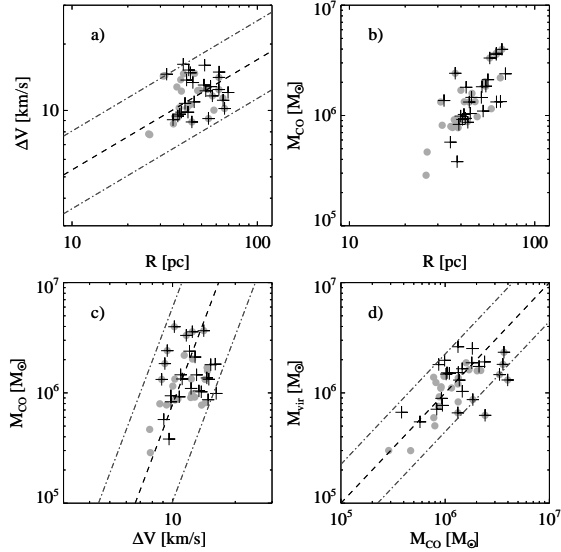


Figure 6. (a) $\Delta V - R$ plot for the identified GMCs. Crosses indicate the values corrected with the Gaussian correction, and gray filled circles indicate the uncorrected values. Broken line indicates the scaling relation of Solomon et al. (1987). For comparison, the scaling relations with different coefficients (multiplied by 1.5 and 1/1.5, respectively) are indicated with dash-dotted lines. (b) Same as (a) but for $M_{\text{CO}} - R$. (c) Same as (a) but for $M_{\text{CO}} - \Delta V$. (d) Same as (a) but for $M_{\text{vir}} - M_{\text{CO}}$.

”wHII” GMCs are located downstream of the ”woHII” GMCs. If the line of $\theta = -13^\circ$ is taken as the partition line, the GMCs upstream and downstream of the line show the difference in terms of the star formation activity. The difference in the star formation activity within each GMC seems to be well related with the position with respect to the spiral arm; while all of the clouds upstream of the line are ”woHII” GMCs, most of the clouds downstream of the line are ”wHII” GMCs. This is in accordance with the prediction of density wave induced/regulated star formation. Hereafter, we will inspect the change of the molecular gas properties according to the classification defined.

3.6. Line ratio

Because of the low critical densities of the ^{13}CO (1-0) and the ^{12}CO (1-0) lines ($n_{\text{H}_2} < 10^3 \text{ cm}^{-3}$) and the large difference of the optical depth between both the lines, the line ratio between both the lines ($I(^{13}\text{CO} (1-0))/I(^{12}\text{CO} (1-0)) \equiv R_{13/12}$) could be used as a probe which distinguishes discrete cloud structures such as ridge of GMCs from diffuse cloud envelopes. It is widely known from the observations of Galactic molecular clouds that while $R_{13/12}$ is high at the center of discrete GMCs (1/3.7; Polk et al. 1988), it is low (1/10–1/20) at the peripheral regions of GMCs (Sakamoto et al. 1994) and in small translucent clouds or diffuse high-

Table 2
Basic Molecular Cloud Properties

ID	Position ^a (arcsec, arcsec)		V_{LSR} (km s ⁻¹)	T_{peak} (Jy beam ⁻¹)	R (pc)	ΔV (km s ⁻¹)	M_{CO} (10 ⁶ M_{\odot})	M_{vir} (10 ⁶ M_{\odot})
1	16.8	-17.7	87.2	0.47	62.0	12.4	3.58	1.81
2	25.0	-23.8	89.5	0.47	57.2	11.6	3.32	1.47
3	15.7	1.8	92.6	0.40	44.3	8.9	1.32	0.66
4	12.6	15.9	93.1	0.44	54.5	9.2	1.84	0.87
5	-5.3	17.0	100.5	0.41	62.0	14.1	3.66	2.34
6	-0.8	11.0	97.0	0.32	32.4	14.6	1.37	1.31
7	23.1	-51.8	79.4	0.62	37.2	9.4	2.42	0.63
8	12.1	-7.6	90.9	0.28	69.5	12.1	2.39	1.91
9	0.4	4.8	87.1	0.27	51.5	13.0	1.46	1.66
10	7.7	-0.9	87.2	0.27	45.6	10.9	1.46	1.03
11	-4.1	30.9	96.3	0.60	66.5	10.2	3.98	1.31
12	2.7	15.3	95.4	0.29	42.6	15.2	1.80	1.87
13	10.3	-17.1	96.6	0.24	52.0	16.0	1.82	2.52
14	23.0	-38.0	84.1	0.29	38.9	9.8	0.83	0.71
15	0.9	-14.4	92.1	0.24	65.3	11.1	1.34	1.53
16	23.6	-33.1	87.9	0.26	43.5	14.8	0.87	1.80
17	1.4	20.9	94.3	0.31	55.9	12.8	2.11	1.74
18	-7.3	8.9	97.3	0.24	44.9	13.4	1.04	1.52
19	13.7	-22.4	93.2	0.22	39.9	16.2	0.99	1.98
20	6.4	8.1	94.1	0.20	52.7	12.3	1.10	1.50
21	1.3	-21.8	93.4	0.21	35.1	9.1	0.57	0.55
22	-9.7	-27.1	90.8	0.29	40.7	10.8	0.92	0.89
23	-20.3	5.0	77.2	0.26	41.5	13.7	1.02	1.48
24	-14.1	9.7	86.2	0.23	42.2	9.8	0.94	0.77
25	-5.2	-4.2	88.5	0.18	62.2	14.9	1.33	2.62
26	31.4	-8.4	92.9	0.18	38.1	9.6	0.38	0.67

^a Offset from 3^h47^m4^s.1, 68°7′26″

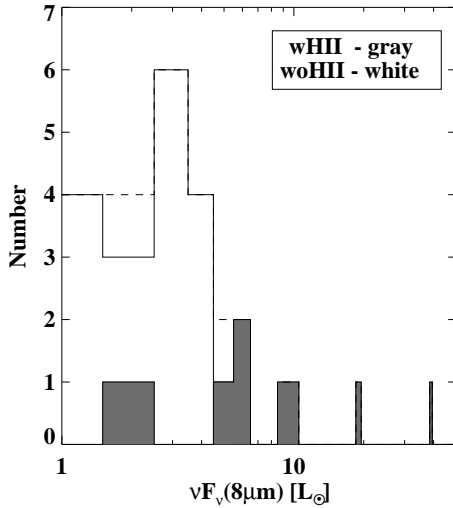


Figure 7. Histogram of the 8 μ m flux measured within each cloud boundary of the "wHII" GMCs (gray area) and the "woHII" GMCs (white area).

latitude clouds (Blitz & Stark 1986; Magnani et al. 1985; Knapp & Bowers 1988).

Previous extended mapping of IC 342 in the ¹³CO (1–0) found that there exist variations of $R_{13/12}$ in the disk of IC 342 (Hirota et al. 2010). $R_{13/12}$ was found to be low (~ 0.1) at the center of the GMA and both the bar ends compared to the other disk regions (0.14–0.2). It was also found that the star formation activity in such low $R_{13/12}$ regions are low compared to the high $R_{13/12}$ regions. The spatial relation between $R_{13/12}$ and the star

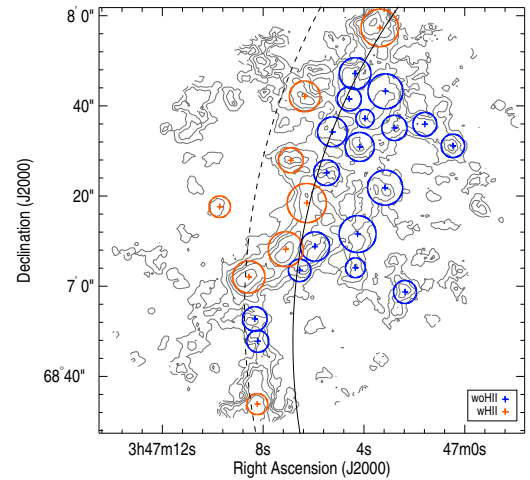


Figure 8. Locations of the identified GMCs superposed on contour map of the velocity integrated ¹²CO (1–0) image. Contour levels of the ¹²CO images are same as in Figure 2. Crosses and circles indicate the locations and the sizes of the GMCs. Radii of the circles are taken as an effective radius of the GMCs. Red markers represent the GMCs associated with H II region ("wHII" clouds), while blue markers represent the GMCs without H II region ("woHII" clouds). Lines of constant spiral phase are indicated with a dashed line ($\phi = 0^\circ$) and a solid line ($\phi = -13^\circ$).

formation suggests that unlike in the starburst galactic centers (e.g., Paglione et al. 2001), the temperature variation is not a main cause of the $R_{13/12}$ variations in the disk region. Likely explanation of the $R_{13/12}$ variations in the disk is that $R_{13/12}$ reflects the fraction of the dif-

fuse molecular component within the beam. The diffuse molecular component refers to molecular cloud with low column and volume densities.

A map of $R_{13/12}$ was made with the following procedures. First, to improve the S/N, both the ^{12}CO and ^{13}CO data cubes were smoothed to $5''$ resolution (~ 80 pc). Next, masking data were made from the ^{12}CO data cube following the same procedure described in Section 3.2 and were applied to the ^{13}CO data cubes. Validity of the mask was checked with the same procedure performed in Section 3.2. Finally, the $R_{13/12}$ value for each point was calculated using the masked data.

Figure 9 shows the map of $R_{13/12}$ compared with the ^{12}CO (1–0) map. $R_{13/12}$ varies over the observed fields from ~ 0.06 to ~ 0.25 . An error of the ratio was estimated following the propagation of the error and was ~ 0.01 at the brightest ^{12}CO peaks (Point 1–3) and typically below 0.02 at the rest. $R_{13/12}$ is rather low on the northern side compared to the southern side. Especially, at the center of the GMA, $R_{13/12}$ marks low value ($\sim 0.06 \pm 0.01$), which is by far small compared to the ridge of GMCs (1/3.7, Polk et al. 1988) and close to the values found in diffuse clouds (Blitz & Stark 1986; Magnani et al. 1985; Knapp & Bowers 1988). On the other hand, southern clouds show higher $R_{13/12}$ ($\sim 0.16 \pm 0.01$), suggesting discrete nature of the clouds.

Comparing the distribution of the "wHII" and "woHII" clouds with the observed $R_{13/12}$ variation shows that there is a possible tendency that while $R_{13/12}$ is lower in the "woHII" GMCs, it is higher in the "wHII" GMCs. The configurations of the $R_{13/12}$ and star formation distributions exclude temperature variation as a primary factor for the $R_{13/12}$ variations. The configurations also likely exclude abundance variation induced by selective photo dissociation of rarer isotopic species. As the observed size scale of the $R_{13/12}$ variation is an order of 100pc, enrichment of ^{13}C through stellar processing conflicts in terms of timescale. Thus, the variation of the $^{13}\text{CO}/^{12}\text{CO}$ abundance ratio is also unlikely. As suggested by Hirota et al. (2010), the most likely explanation for the $R_{13/12}$ variation in the disk of IC 342 is the variation of fraction of the diffuse molecular component. Formation of dense cloud core ($n_{\text{H}_2} \sim 10^6 \text{ cm}^{-2}$) is required for the onset of star formation. Very low $R_{13/12}$ values found at the locations of some of the "woHII" GMCs ($R_{13/12} < 0.1$) suggest that those "woHII" GMCs contain large fraction of diffuse cloud components and thus lower fraction of cloud cores compared to the "wHII" GMCs.

4. DISCUSSION

4.1. Change of Cloud Property Across the Spiral Arm

The offset between the molecular gas traced by the $^{12}\text{CO}(1-0)$ emission and massive star forming regions is often seen in grand-design spiral galaxies (e.g., Vogel et al. 1988; Rand et al. 1992; Rand 1995). Typical extent of the spatial offsets between the two components are typically 100–300 pc. However, most of the previous observations for such grand-design spiral galaxies, which are beyond the Local Group of galaxies, were at resolutions of 200–1000 pc and were insufficient to investigate the variation of the molecular gas properties within these

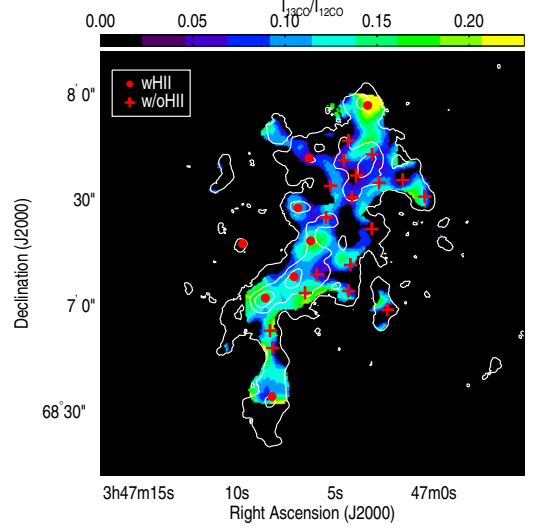


Figure 9. Color representation of $R_{13/12}$ superposed by contour map of ^{12}CO (1–0) image. Contour levels are 1, 3, 5, and 7 times $1.5 \text{ Jy beam}^{-1} \text{ km s}^{-1}$. Both images were made from the data cube smoothed to $5''$ resolution. Locations of the "wHII" and the "woHII" GMCs are indicated with filled circles and crosses, respectively. Errors of the $R_{13/12}$ are typically ~ 0.01 at the bright peaks and ~ 0.02 at the rest regions.

offsets. The NMA+45m combined data provide a unique opportunity to look into the process involved there with a resolution of ~ 50 pc and an improved sensitivity to the extended diffuse emission.

Figure 10 shows scatter plots of the properties of clouds for each category. The $R - \Delta V$ plot (Figure 10(a)) shows that "woHII" GMCs have larger line width compared to the "wHII" GMCs with the same size. The Kolmogorov–Smirnov test was performed to the ratio between R and ΔV with a null hypothesis of both categories being extracted from the same parent sample. The null hypothesis was rejected with a p -value of ~ 0.004 . A similar trend is also seen in the $\Delta V - M_{\text{CO}}$ plot (Figure 10(b)). Again, the Kolmogorov–Smirnov test was performed and indicated that there is a significant difference between the both categories with a p -value of ~ 0.001 . Another difference of properties between the "wHII" and the "woHII" GMCs is seen in the $M_{\text{CO}} - M_{\text{vir}}$ plot (Figure 10(c)). There is a tendency that the "woHII" GMCs have a larger virial mass to luminosity mass ratio than the "wHII" GMCs ($p \sim 0.001$), suggesting that "woHII" clouds are less gravitationally bound compared to the "wHII" clouds.

Figure 11 shows histograms of the basic properties of the clouds (radius, line width, and mass). While a little difference between the two categories is seen in the radius histogram, apparent differences are seen in the mass and the line width histograms. As we have seen in the previous scatter plots, the line width distribution of the "woHII" GMCs seems to be different from the "wHII" GMCs ($p \sim 0.017$, for the Kolmogorov–Smirnov test). The median line width of the "woHII" GMCs is $\sim 13.4 \text{ km s}^{-1}$ and is larger than that of the "wHII" GMCs ($\sim 10.2 \text{ km s}^{-1}$). Two cloud categories also show difference in the mass histogram ($p \sim 0.011$). The mass of the "woHII" GMCs is concentrated around the median value of $1.3 \times 10^6 M_{\odot}$, except for the cloud-5 with the

mass of $\sim 3.7 \times 10^6 M_\odot$, which is located at the center of the GMA. On the contrary, the mass distribution of the "wHII" GMCs is more widely spread and stretched to a higher mass regime, up to $4.0 \times 10^6 M_\odot$. Except for a cloud-26, all masses of "wHII" GMCs are larger than $10^6 M_\odot$. The cloud-26, which is located ~ 300 pc downstream from the molecular ridge, has mass of $0.4 \times 10^6 M_\odot$ and is likely being disrupted by feedback from associating H II regions.

The comparison between the cloud properties between the two cloud groups (the "wHII" and the "woHII" GMCs) indicated significant variation of cloud properties according to their associated star forming activity. The "woHII" GMCs have larger line width and have smaller mass and moreover, are less gravitationally bound compared to the "wHII" GMCs. Spatial distribution of the clouds indicate that the "wHII" GMCs are located downstream of the "woHII" GMCs, on average. These facts suggest that cloud properties do change by crossing the spiral arm.

4.2. Effect of Gas Velocity Dispersion

The comparison between the virial mass and the luminosity-based mass made in the previous subsection indicated that the "woHII" GMCs are loosely bound compared to the "wHII". The degree of gravitational binding can be expressed with a virial parameter, (α_{vir} : Bertoldi & McKee 1992), which is expressed by

$$\alpha_{\text{vir}} = M_{\text{vir}}/M_{\text{CO}}. \quad (6)$$

As α_{vir} decreases, cloud gets more unstable against gravitational collapse. In this subsection, we will utilize α_{vir} to investigate which of the cloud properties is responsible for the observed variation of the gravitational instability of the clouds.

Figure 12 shows the scatter plots between the basic cloud properties and α_{vir} . To see whether there exist a significant relation between the virial parameter α_{vir} with other cloud properties, Kendall's τ and associated probability of chance correlation were calculated. Significant correlation was only detected between the virial parameter α_{vir} and the line width ($p \sim 6.0 \times 10^{-6}$). GMCs in the Galactic center exhibit similar correlation between the line width and the degree of gravitational binding (Oka et al. 2001). The correlation suggests that the degree of gravitational binding of the clouds is mainly determined by their internal turbulent motion.

The "wHII" GMCs have smaller velocity dispersion and α_{vir} , and located downstream compared to the "woHII" GMCs. Similar relation between the star formation activity and the line width was pointed out by Kohno et al. (1999). They found an anticorrelation between the dense molecular gas fraction and the line width in the center of the barred galaxy NGC 6951, with a spatial resolution of ~ 400 pc. The results presented here suggest that the anticorrelation between the star formation and the line width holds down to the size scale of GMC. It is tempting to consider that dissipation of turbulent motion inside the GMCs occurs by crossing the spiral arm, and leads to the subsequent massive star formation.

We must note that Scoville et al. (1986) indicated the relation between the star formation activity and the line width, but in an opposite sense; GMCs smaller than 40 pc

show that the GMCs associated with H II regions have larger line width compared to the GMCs without H II regions. The difference in the results is likely due to the difference in the observed size scales. Since the spatial resolution of the data used by Scoville et al. (1986) is finer than this work (down to pc scale), the effects of local phenomena, such as shock induced by cloud-cloud collision and radiation feed backs from H II regions, might be dominant in the previous result. While, on the other hand, the resolution of this study is comparable to the size of the GMCs and the derived properties should be reflecting the 'global' properties of clouds rather than the internal phenomena within each cloud.

4.3. Evolution of GMC in the Spiral Arm

The results presented in the previous subsections illustrated the variations of the cloud properties across the spiral arm in IC 342. The "wHII" (downstream) GMCs are more virialized and massive compared to the "woHII" (upstream) GMCs. The cloud groups also differ from each other in that the velocity dispersion of the "wHII" GMCs is larger than that of the "woHII" GMCs. In this subsection, we will discuss the implications of such variations of the cloud properties.

First question is from what kind of material the clouds identified in this study were made? There are two classes of concepts about the formation of GMCs in the spiral arm. One is that GMCs are formed from H I clouds in the inter-arm and another is that GMCs are built-up from smaller clouds in the inter-arm through agglomeration. As we have seen before in Section 3.3.2, the surface mass density of H I is only $\sim 2 M_\odot \text{ pc}^{-2}$ within the observed region. On the other hand, the surface mass density of the molecular gas is estimated to be $\sim 30 M_\odot \text{ pc}^{-2}$ from the single-dish ^{12}CO data. So, it is natural to consider that the GMCs in the spiral arm are formed from the pre-existing molecular clouds.

As the extent of the observed region is limited, we are unable to tell the nature of the inter-arm molecular clouds from the observed data alone. Instead, we refer to the observations of molecular clouds in the Milky Way. It is known that GMC with mass above $10^5 M_\odot$ is rarely seen in the inter-arm region (e.g., Sanders et al. 1985). Heyer et al. (1998) indicated that inter-arm molecular clouds are smaller than $3 \times 10^4 M_\odot$ and not virialized in the outer Galaxy. Even in the molecular-rich inner Galaxy, there are substantial contributions of diffuse molecular emission, suggesting the existence of small clouds. (Polk et al. 1988; Chiar et al. 1994). It seems natural to assume that inter-arm molecular clouds are dominated by the small molecular clouds.

Second question is what kind of mechanism could explain the observed variations of cloud properties? If the inter-arm clouds in IC 342 are small, diffuse clouds, the mechanism for building up the GMCs as massive as $10^6 M_\odot$ must exist. The timescale for building up should be comparable to the arm crossing time in this region ($t_{\text{arm}} \sim 3 \times 10^7 \text{ yr}$, Hirota et al. 2010). The random coalescence of molecular clouds is proposed as a formation mechanism of GMC (Kwan & Valdes 1983; Casoli & Combes 1982; Tomisaka 1984; Roberts & Stewart 1987; Elmegreen 1990; Dobbs 2008). Early calculations indicated that it may take

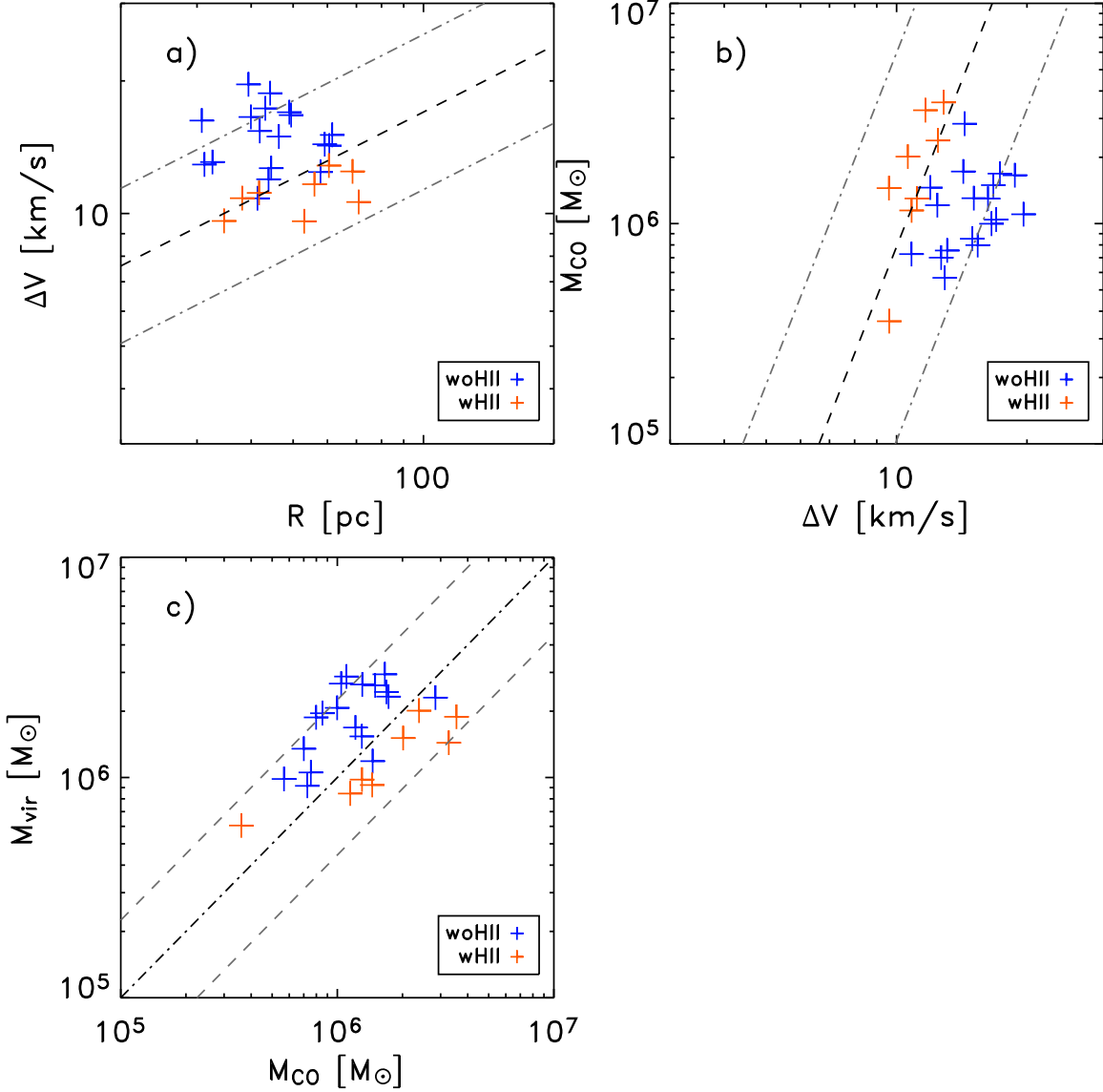


Figure 10. a) $\Delta V - R$ plot of the identified GMCs. Red and blue crosses indicate the "wHII" GMCs and the "woHII" GMCs, respectively. Broken line indicates the scaling relation of Solomon et al. (1987). For comparison, the scaling relations with different coefficients (multiplied by 1.5 and 1/1.5, respectively) are indicated with dash-dot lines. b) same as a), but for $M_{CO} - \Delta V$. c) same as a), but for $M_{vir} - M_{CO}$.

about 10^8 yr, which is far longer than t_{arm} . However, if the spiral density waves are included, it turns out that the formation of the GMC as massive as several times $10^6 M_{\odot}$ within a time comparable with t_{arm} is possible. Large-scale instability induced by the self-gravity of gas shall further make the agglomeration process efficient (e.g., Balbus & Cowie 1985; Dobbs 2008).

If the random coalescence model is adopted, the observed nature of the "wHII" and the "woHII" GMCs could be understood naturally. GMCs were made from the small molecular cloud in the inter-arm through agglomeration. The end product of the cloud growth will be the "wHII" ("post arm") GMCs, which have masses of $(1-3) \times 10^6 M_{\odot}$ (an exception is the cloud-26). As the masses of the "woHII" GMCs are around $10^6 M_{\odot}$ and smaller compared to the "wHII" GMCs, it may be natural to consider that the "woHII" GMCs are at the intermediate stage of the cloud growth by coalescence. The relatively low peak temperatures of the "woHII" GMCs ($T_{MB} = 2-3$ K) and

the low degree of gravitational binding ($\alpha_{vir} = 1-3$) are in agreement with the notion that the "woHII" GMCs are collective of smaller clouds, which are yet not virialized.

Above interpretation may be in agreement with the recent results of observations of the grand-design spiral galaxy M51. Koda et al. (2009) performed full aperture observation of M51 in ^{12}CO (1-0) with a spatial resolution of ~ 200 pc and indicated that while massive GMAs are preferentially found in the spiral arm, GMCs with mass below $10^6 M_{\odot}$ are uniformly distributed over the molecular gas disk. Egusa et al. (2011) carried out CO observations toward the selected region of M51 with a spatial resolution of 30 pc, comparable with ours, but not corrected for missing-flux, and found that clumps with mass of $10^5-10^6 M_{\odot}$ are likely preferentially located on the downstream side of the spiral arm. The combined data presented here revealed while rather diffuse "woHII" clouds are the present at the upstream side,

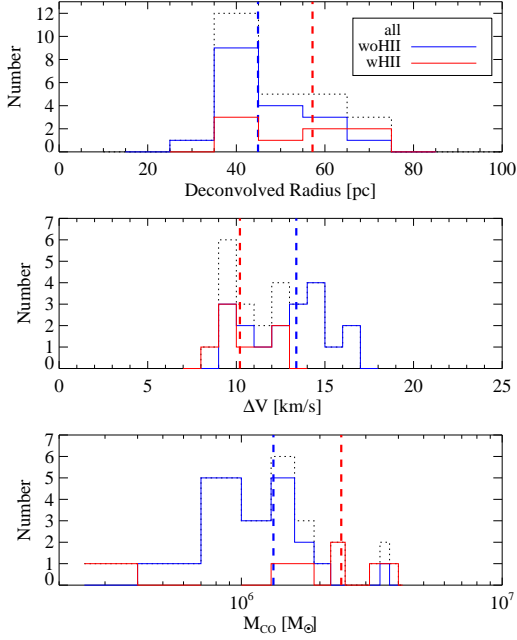


Figure 11. Histogram of the basic properties of the GMCs, namely, deconvolved effective radius, deconvolved line width, and luminosity mass. Histograms for the “wHII” GMCs, the “woHII” GMCs, and all GMCs are indicated with red solid, blue solid, and dotted lines, respectively. Vertical dashed lines in red and blue indicate the median value of each category.

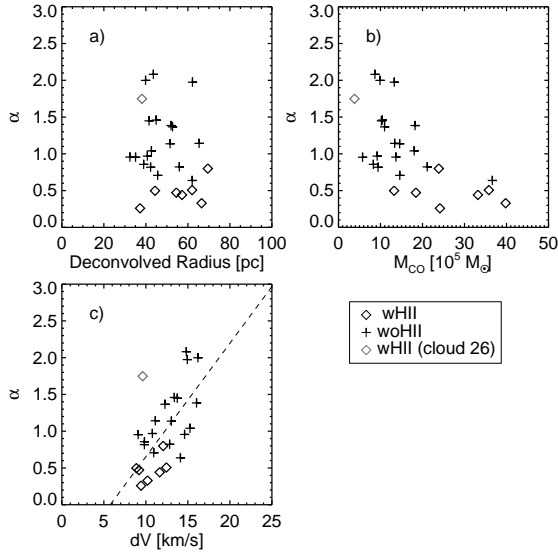


Figure 12. (a) Relationship between the virial parameter ($\alpha_{\text{vir}} \equiv M_{\text{vir}}/M_{\text{CO}}$) and radius (R). Crosses indicate the “wHII” GMCs and open triangles indicate the “woHII” GMCs. A gray cross represents the cloud-26. (b) Same as (a), but for α_{vir} and M_{CO} . (c) Same as (a), but for α_{vir} and ΔV . Dashed line indicates a linear fit between the two quantities.

discrete clouds are seen on the downstream side. While the buildup of GMAs by coagulation of GMCs in the inter-arm of M51 was suggested by Koda et al. (2009), the low $R_{13/12}$ in the center of the GMA and presence of diffuse clouds in the upstream of the spiral arm implies coalescence of diffuse clouds are much important in the

arm of IC 342.

Another important aspect of the variation of cloud properties is the decrease of line width. Since molecular clouds collide inelastically, part of the kinetic energy should be transformed into thermal energy and radiated. Tomisaka (1987) carried out the numerical simulation of collisional clouds incorporating formation and destruction of GMCs, the loss of random velocity due to inelastic cloud collision, and the energy input by the star formation within GMCs. The results were that after the compression of cloud by the shock, random velocity of clouds decreases and density increases. These are in agreement with the results presented in previous subsections.

The scenario of cloud growth would be summarized as follows. First, the inter-arm molecular clouds are collected because of the convergence of stream line before the spiral arm. Due to this convergence of stream line and self-gravity, clouds will stick and form the cloud collective with masses of $10^6 M_{\odot}$, although they are not fully virialized yet and loosely bound. These cloud collectives are observed as the “woHII” GMCs. Once massive GMC is formed, its large gravitational cross section accelerates the coalescence and swallows diffuse clouds at the envelope. The excess kinetic energy will be dissipated due to inelastic collision and virialized GMCs with mass larger than $10^6 M_{\odot}$ are formed (the “wHII” GMCs”).

4.4. Condition of Massive Star Formation

The closeness between the star forming regions and the “wHII” GMCs suggests that these clouds are real progenitors of the associated H II regions. This can also be justified by the consideration of the age of H II regions. Sizes of the H II regions seen in the H α image have at most a diameter of ~ 100 pc. Assuming sound speed in the ionized gas as $c \sim 10$ km s $^{-1}$, an upper limit on the age of the H II regions could be estimated as $D/2c = 5$ Myr. As the age of H II regions estimated is much shorter than the arm crossing time ($t_{\text{arm}} \sim 3 \times 10^7$ Myr), the H II regions must have been born within the associated “wHII” GMCs on site. The relatively young age of the H II regions compared to t_{arm} gives us another important implication; if the “woHII” GMCs are able to initiate massive star formation, we should see the symptoms of massive star formation inside the “woHII” GMCs. Nevertheless, little $8\mu\text{m}$ emission could be seen in the “woHII” GMCs. This implies that there must be a condition for massive star formation, which is fulfilled by the “wHII” GMCs but not by the “woHII” GMCs.

As we have seen in Section 4.3, collisional coagulation of clouds seems to be responsible for the evolution of the GMCs. One of the possible mechanism for initiating massive star formation is cloud–cloud collision (Scoville et al. 1986; Tan 2000). In this picture, molecular clouds are compressed by the shock at the colliding surface and subsequently dense cores are formed (Kimura & Tosa 1996). However, at the center of the GMA where large velocity gradient due to streaming motions is observed and enhanced rate of collision is expected, little or no sign of star formation is seen. This implies that for the onset of massive star formation, not only cloud collision but also some other conditions may be required. Another interpretation as following might arise. Namely, after star formation is initiated inside the “woHII” clouds, star formation proceeds rather slowly

and become only visible at the "wHII" clouds. However, this requires slow progress of star formation, with a timescale comparable to the arm-crossing time mentioned above. Even if this is the case, the progress of the star formation shall be regulated by the evolution of GMCs because of the far longer timescale of arm-crossing time compared to dynamical timescale in each GMC ($\sim 4 \times 10^6$ yr, e.g., Pringle et al. 2001). Both interpretations require the evolution of the cloud properties which enable triggering of star formation to work effectively.

Figure 13 shows a scatter plot of the area-averaged $8\mu\text{m}$ luminosity measured within each cloud boundary and the virial parameter α_{vir} for each cloud. There is a tendency that $8\mu\text{m}$ luminosity, which is proportional to the star formation rate, is higher in the range of $\alpha_{\text{vir}} < 1$ compared to in the range of $\alpha_{\text{vir}} > 1$. It was shown in Section 4.2 that the degree of binding of the GMCs is mainly determined by its line width. These facts suggest that virialization of GMC achieved by the dissipation of turbulent motion is one of the necessary conditions for the onset of massive star formation.

Recent studies emphasize the importance of turbulence in both regulating and the triggering star formation. In the theory of turbulence regulated star formation, although dense cores are formed by the shock driven by supersonic turbulence inside a GMC (e.g., Padoan & Nordlund 2002; Mac Low & Klessen 2004), limited part of the GMC can be dense enough to form cloud cores since the greater part of the GMC are supported by the excess kinetic energy (Elmegreen 2002). Krumholz & McKee (2005) presented semianalytical calculation using the theory and showed that amount of the excess kinetic energy inside the GMC, which is proportional to α_{vir} , controls the production rate of cloud cores, and thus star formation rate. This point is in agreement with our results that dissipation of turbulence is required for the onset of massive star formation. After GMCs have dissipated excess kinetic energy, it can initiate star formation, whatever the trigger may be.

5. SUMMARY

Results of the full aperture observations of the north-eastern spiral arm segments of IC 342 in ^{12}CO (1–0) and ^{13}CO (1–0) made with a spatial resolution of ~ 50 pc were presented. Though the spatial resolution of the observations is not high enough to resolve internal structure of GMCs, it is capable of investigating the global property of massive GMCs. The observations cover the $1\text{kpc} \times 1.5\text{kpc}$ region which contain a GMA with mass of $\sim 10^7 M_{\odot}$, where spatial offsets between ^{12}CO and star-forming regions exist. The NMA data were combined with the 45m telescope data to image the extended CO distribution and investigate whether and how the properties of molecular clouds change by crossing the spiral arm. The results are summarized as follows.

1. The spiral arms were resolved into a number of clouds which have size, temperature, and surface mass density comparable to the massive GMCs in the Galaxy. While the ^{12}CO (1–0) distribution is concentrated in a narrow ridge in the southern half of the observation field, it is more smoothly distributed in the northern half, where the GMA

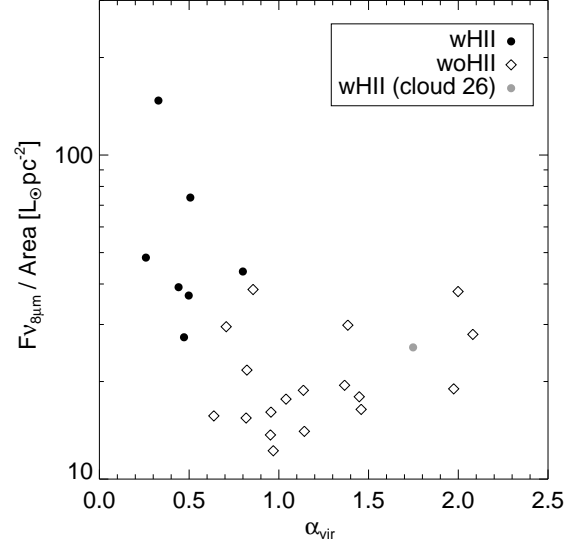


Figure 13. Scatter plot of area-averaged $8\mu\text{m}$ luminosity measured within each cloud boundary and the virial parameter (α_{vir}) for each cloud. Filled circles indicate the "wHII" GMCs, open diamonds the "woHII" GMCs, and filled gray circle indicates the cloud-26.

exists. Comparison with the ^{13}CO (1–0) image showed that at the center of the GMA only little ^{13}CO (1–0) emission is detected despite of its strong ^{12}CO emission.

2. Comparison with star formation tracers indicated that while some of the clouds are closely associated with star forming regions, the rest of the clouds show little or no sign of massive star formation. The identified clouds were divided into two categories according to whether they are associated with star formation activity or not.
3. Twenty-six clouds with masses of $(0.4\text{--}3.7) \times 10^6 M_{\odot}$ were identified from the ^{12}CO (1–0) data cube. The size and the line width of the clouds were comparable to GMCs in the Milky Way. The identified clouds also followed the linewidth–size relation and the mass–linewidth relation of the Galactic GMCs, suggesting that the identified clouds are resemblance of Galactic GMCs.
4. The identified clouds (GMCs) were divided into two categories according to whether they are associated with star-forming regions or not. Comparison between both categories showed that clouds which are associated with star-forming regions ("wHII" GMCs) are more virialized and massive compared to the clouds which show little or no sign of star formation ("woHII" GMCs). Moreover, the "woHII" GMCs have larger line width compared to the "wHII" GMCs. As the "wHII" GMCs are located downstream of the "woHII" GMCs, it is concluded that properties of the GMCs do change by crossing the spiral arm.
5. The line ratio, $R_{13/12}$, varies from 0.06 ± 0.01 in the center of the GMA where little or no sign of star formation is seen to ~ 0.16 in the discrete

GMCs which are associated with H II regions. On the whole, the "woHII" GMCs likely show a low $R_{13/12}$ value which suggests a larger fraction of diffuse molecular cloud components than the "wHII" GMCs.

6. To see what parameter of the GMC controls degree of gravitational boundness of the GMC, correlation plots between the virial parameter, $\alpha_{\text{vir}} = M_{\text{vir}}/M_{\text{CO}}$, and other basic GMC properties, namely, radius, line width, and mass were made. The linewidth- α_{vir} plot indicated most strong correlation implying that the dissipation of turbulent motion controls the boundness of the GMCs.
7. Random coagulation of the pre-existing small clouds can explain the growth of the mass and the timescale involved in the change. Collisional coalescence involved in random coagulation may also explain the observed decrease of line width, as the kinetic energy of the clouds will be dissipated by inelastic cloud collision.
8. The closeness of H II regions and the "wHII" GMCs imply that those GMCs are real progenitors of the associated H II regions. The rough estimate of the age of H II regions gives ~ 5 Myr, which is well below the arm-crossing time. This implies if the "woHII" GMCs are able to initiate star formation, the symptoms should have seen. So, the sparseness of star formation in the "woHII" GMCs suggests they do not meet the condition for massive star formation.

Plot of area-averaged $8\mu\text{m}$ luminosity and virial parameter (α_{vir}) shows a tendency that the $8\mu\text{m}$ luminosity, which is proportional to the star formation rate, rises in the range of $\alpha_{\text{vir}} < 1$. This might imply that dissipation of turbulence controls not only the evolution of GMCs, but also the probability of massive star formation.

The authors would like to thank the Nobeyama Radio Observatory (NRO) staff for operating the NMA and the 45m telescope. NRO is a division of the National Astronomical Observatory of Japan under the National Institutes of Natural Science.

Facilities: No:45m, NoMA ()

REFERENCES

- Balbus, S. A., & Cowie, L. L. 1985, *ApJ*, 297, 61
 Becklin, E. E., Gatley, I., Matthews, K., Neugebauer, G., Sellgren, K., Werner, M. W., & Wynn-Williams, C. G. 1980, *ApJ*, 236, 441
 Bertoldi, F., & McKee, C. F. 1992, *ApJ*, 395, 140
 Blitz, L. 1993, *Protostars and Planets III*, ed. E. Levy, J. I. Lunine, & T. M. Bania (Tucson, AZ: Univ. Arizona Press), 125
 Blitz, L., & Stark, A. A. 1986, *ApJ*, 300, L89
 Blitz, L., & Thaddeus, P. 1980, *ApJ*, 241, 676
 Bolatto, A. D., Leroy, A., Israel, F. P., & Jackson, J. M. 2003, *ApJ*, 595, 167
 Bonnell, I. A., & Bate, M. R. 2006, *MNRAS*, 370, 488
 Bonnell, I. A., Bate, M. R., Clarke, C. J., & Pringle, J. E. 2001, *MNRAS*, 323, 785
 Calzetti, D., et al. 2005, *ApJ*, 633, 871
 Calzetti, D., et al. 2007, *ApJ*, 666, 870
 Casoli, F., & Combes, F. 1982, *A&A*, 110, 287
 Chiar, J. E., Kutner, M. L., Verter, F., & Leous, J. 1994, *ApJ*, 431, 658
 Crosthwaite, L. P., Turner, J. L., & Ho, P. T. P. 2000, *AJ*, 119, 1720
 Crosthwaite, L. P., Turner, J. L., Hurt, R. L., Levine, D. A., Martin, R. N., & Ho, P. T. P. 2001, *AJ*, 122, 797
 Dame, T. M., Elmegreen, B. G., Cohen, R. S., & Thaddeus, P. 1986, *ApJ*, 305, 892
 Dame, T. M., Hartmann, D., & Thaddeus, P. 2005, *ApJ*, 547, 792
 de Vaucouleurs, G., de Vaucouleurs, A., Corwin, H. G., Jr., Buta, R. J., Paturel, G., & Fouqu, P. 1991, *Third Reference Catalogue of Bright Galaxies Vols. 1-3, XII* (New York: Springer), 2069
 Dobbs, C. L. 2008, *MNRAS*, 391, 844
 Eckart, A., Downes, D., Genzel, R., Harris, A. I., Jaffe, D. T., & Wild, W. 1990, *ApJ*, 348, 434
 Egusa, F., Koda, J., & Scoville, N. 2011, *ApJ*, 726, 85
 Elmegreen, B. G. 1990, in *ASP Conf. Ser. 12, The Evolution of the Interstellar Medium*, ed. L. Blitz (San Francisco: ASP), 247
 Elmegreen, B. G. 2002, *ApJ*, 577, 206
 Fazio, G. G., et al. 2004, *ApJS*, 154, 10
 Helou, G., et al. 2004, *ApJS*, 154, 253
 Hernandez, O., Carignan, C., Amram, P., Chemin, L., & Daigle, O. 2005, *MNRAS*, 360, 1201
 Heyer, M. H., & Brunt, C. M. 2004, *ApJ*, 615, L45
 Heyer, M. H., Brunt, C., Snell, R. L., Howe, J. E., Schloerb, F. P., & Carpenter, J. M. 1998, *ApJS*, 115, 241
 Hirota, A., Kuno, N., Sato, N., Nakanishi, H., Tosaki, T., & Sorai, K. 2010, *PASJ*, 62, 1261
 Ishizuki, S., Kawabe, R., Ishiguro, M., Okumura, S. K., & Morita, K.-I. 1990, *Nature*, 344, 224
 Israel, F. P., & Baas, F. 2003, *A&A*, 404, 495
 Jarrett, T. H., Chester, T., Cutri, R., Schneider, S. E., & Huchra, J. P. 2003, *AJ*, 125, 525
 Kimura, T., & Tosa, M. 1996, *A&A*, 308, 979
 Knapp, G. R., & Bowers, P. F. 1988, *ApJ*, 331, 974
 Koda, J., Sawada, T., Hasegawa, T., & Scoville, N. Z. 2006, *ApJ*, 638, 191
 Koda, J., et al. 2009, *ApJ*, 700, L132
 Kohno, K., Kawabe, R., & Vila-Vilaró, B. 1999, *ApJ*, 511, 157
 Krumholz, M. R., & McKee, C. F. 2005, *ApJ*, 630, 250
 Kuno, N., et al. 2007, *PASJ*, 59, 117
 Kurono, Y., Morita, K.-I., & Kamazaki, T. 2009, *PASJ*, 61, 873
 Kwan, J., & Valdes, F. 1983, *ApJ*, 271, 604
 Larson, R. B. 1981, *MNRAS*, 194, 809
 MacLaren, I., Richardson, K. M., & Wolfendale, A. W. 1988, *ApJ*, 333, 821
 Mac Low, M.-M., & Klessen, R. S. 2004, *Reviews of Modern Physics*, 76, 125
 Maddalena, R. J., & Thaddeus, P. 1985, *ApJ*, 294, 231
 Magnani, L., Blitz, L., & Mundy, L. 1985, *ApJ*, 295, 402
 Meier, D. S., & Turner, J. L. 2005, *ApJ*, 618, 259
 Meier, D. S., Turner, J. L., & Hurt, R. L. 2000, *ApJ*, 531, 200
 Oka, T., Hasegawa, T., Sato, F., Tsuboi, M., Miyazaki, A., & Sugimoto, M. 2001, *ApJ*, 562, 348
 Okumura, S. K., et al. 2000, *PASJ*, 52, 393
 Padoan, P., & Nordlund, Å. 2002, *ApJ*, 576, 870
 Paglione, T. A. D., et al. 2001, *ApJS*, 135, 183
 Polk, K. S., Knapp, G. R., Stark, A. A., & Wilson, R. W. 1988, *ApJ*, 332, 432
 Pringle, J. E., Allen, R. J., & Lubow, S. H. 2001, *MNRAS*, 327, 663
 Rand, R. J. 1993, *ApJ*, 404, 593
 Rand, R. J. 1995, *AJ*, 109, 2444
 Rand, R. J., Kulkarni, S. R., & Rice, W. 1992, *ApJ*, 390, 66
 Rand, R. J., Lord, S. D., & Higdon, J. L. 1999, *ApJ*, 513, 720
 Rieke, G. H., et al. 2004, *ApJS*, 154, 25
 Roberts, W. W., Jr., & Stewart, G. R. 1987, *ApJ*, 314, 10
 Rosolowsky, E. 2007, *ApJ*, 654, 240
 Rosolowsky, E., & Blitz, L. 2005, *ApJ*, 623, 826
 Rosolowsky, E., Engargiola, G., Plambeck, R., & Blitz, L. 2003, *ApJ*, 599, 258
 Rosolowsky, E., & Leroy, A. 2006, *PASP*, 118, 590

- Sage, L. J., & Solomon, P. M. 1991, *ApJ*, 380, 392
- Saha, A., Claver, J., & Hoessel, J. G. 2002, *AJ*, 124, 839
- Sakamoto, S., Hayashi, M., Hasegawa, T., Handa, T., & Oka, T. 1994, *ApJ*, 425, 641
- Sanders, D. B., Scoville, N. Z., & Solomon, P. M. 1985, *ApJ*, 289, 373
- Sato, N. 2006, PhD Thesis, Hokkaido University
- Sault, R. J., Teuben, P. J., & Wright, M. C. H. 1995, in ASP Conf. Ser. 77, *Astronomical Data Analysis Software and Systems IV*, ed. R. A. Shaw, H. E. Payne, & J. J. E. Hayes (San Francisco, CA: ASP), 433
- Schinnerer, E., Böker, T., Meier, D. S., & Calzetti, D. 2008, *ApJ*, 684, L21
- Schulz, A., Güsten, R., Köster, B., & Krause, D. 2001, *A&A*, 371, 25
- Scoville, N. Z., Sanders, D. B., & Clemens, D. P. 1986, *ApJ*, 310, L77
- Solomon, P. M., Rivolo, A. R., Barrett, J., & Yahil, A. 1987, *ApJ*, 319, 730
- Strong, A. W., & Mattox, J. R. 1996, *A&A*, 308, L21
- Takakuwa, S., Kamazaki, T., Saito, M., & Hirano, N. 2003, *ApJ*, 584, 818
- Tan, J. C. 2000, *ApJ*, 536, 173
- Tomisaka, K. 1984, *PASJ*, 36, 457
- Tomisaka, K. 1987, *PASJ*, 39, 109
- Tsutsumi, T., Morita, K.-I., & Umeyama, S. 1997, in ASP Conf. Ser. 125, *Astronomical Data Analysis Software and Systems VI*, ed. G. Hunt & H. E. Payne (San Francisco, CA: ASP), 50
- Turner, J. L., & Hurt, R. L. 1992, *ApJ*, 384, 72
- Turner, J. L., Hurt, R. L., & Hudson, D. Y. 1993, *ApJ*, 413, L19
- Usero, A., García-Burillo, S., Martín-Pintado, J., Fuente, A., & Neri, R. 2006, *A&A*, 448, 457
- Vazquez-Semadeni, E. 1994, *ApJ*, 423, 681
- Vogel, S. N., Kulkarni, S. R., & Scoville, N. Z. 1988, *Nature*, 334, 402
- Wall, W. F., & Jaffe, D. T. 1990, *ApJ*, 361, L45
- Williams, J. P., de Geus, E. J., & Blitz, L. 1994, *ApJ*, 428, 693